

Modeling plant disease spread via high-resolution human mobility networks

Varun K. Rao,^{1,2} Ryan Higgs,³ Hautahi Kingi,³ Filippo Radicchi,¹ Santo Fortunato,¹ and Maria Litvinova^{2,*}

¹*Center for Complex Networks and Systems Research,
Luddy School of Informatics, Computing, and Engineering,
Indiana University, Bloomington, Indiana 47408, USA*

²*School of Public Health, Indiana University, Bloomington, Indiana 47408, USA*

³*Onside, Christchurch, New Zealand.*

Human mobility plays a crucial role in the spread of human diseases, but is rarely quantified in plant disease epidemics. To address this gap, we integrate a unique, high-resolution network of human movements in New Zealand with a metapopulation model to mechanistically simulate pathogen transmission. We calibrate the model on the nationwide 2010 kiwifruit vine disease (Psa-V) outbreak, and show that it accurately reproduces the observed spatiotemporal spread, confirming that the human mobility network is a strong foundation for modeling transmission dynamics. By analyzing spatial infection trends, we find that most dispersal occurs locally, as often illustrated in the plant-outbreak literature. However, sporadic long-range connections are necessary to model a nationwide outbreak. Using the model as an in-silico laboratory, we demonstrate that enhanced surveillance accelerates detection and that outbreak severity is highly sensitive to the timing and location of initial disease importation. We observe a potential causal link between seasonal labor patterns and epidemic risk in high-traffic seasons. This study provides a robust, data-driven framework for modeling and predicting the spatiotemporal spread of agricultural pathogens. It underscores the importance of leveraging human mobility networks to design timely interventions and surveillance systems, protecting global food security.

I. INTRODUCTION

Direct and indirect impacts of human infections on population health and economic well-being captured the attention of scientific and general audiences in recent years, overshadowing the impact of plant disease outbreaks on national and international biosecurity. Based on a review conducted by Fielder *et al.* [1], at least 38 new plant pathogens were identified, while 10 global plant outbreaks in 2023 challenged crop production, food prices, and food security. Predicting the dynamics of plant disease outbreaks, and consequently responding to these persistent threats, is becoming increasingly complex [2] due to changes in pathogens, their hosts, climate, and human behaviors. Because plant pathogens spread via wind, rain, and insects, studies have emphasized environment-related landscape modeling studies that simulate host-pathogen interactions. These landscape-focused studies use a variety of approaches, including lattice-based models using kernel functions for dispersal [3–11], weather-related statistical modeling [12, 13], Bayesian methods [14, 15], meta-population modeling [9, 16], and mean-field approximations [17] to understand and predict the spread of these pathogens. However, with growing connectivity, human-mediated spread through contaminated equipment and transport [18–20], infected plant material [21], or global trade [22] has become an important force in driving rapid, medium- and long-distance transmission events.

Nevertheless, there are few studies investigating and modeling the impact of human mobility [23–27] on the

long-distance spread of plant-related pathogens [22, 28]. Other works studying long-distance spread have focused on weather-related spread [29, 30]. The few existing studies concerning the role of between-property mobility networks focus on trading [23–25], transport networks [26, 27], or geographical distance [31, 32]. However, these studies use static networks to model spread, and do not account for the temporal changes in the magnitude of the traffic between the properties. Using inspiration from studies modeling spreading processes on temporal networks of livestock movements we represent snapshots of movements at different time periods [33–36] to fill this gap. We propose a multi-scale meta-population model based on empirical network data of human mobility between agricultural properties. Our approach combines lattice model for within-property spread and create a mobility-based network model for between-property spread.

Our work eliminates the main barrier to integrating human mobility into plant disease epidemiology: the lack of high-quality spatiotemporal data suitable for predictive modeling. Our unique dataset for the horticulture industry of New Zealand provides time-stamped origin-destination data for movements between properties. The data was provided and managed by Onside, an agritech company with biosecurity technology covering more than 20,000 properties from multiple industries across several countries, including New Zealand and Australia.

We leverage a Susceptible-Infected metapopulation model [37] to describe plant disease dynamics and calibrate the model to replicate the timing and severity of a past outbreak of *Pseudomonas syringae* *pv.* *actinodiae* (Psa-V) [38]; a bacterial disease that was introduced to New Zealand in 2010 and is still present and

* malitv@iu.edu

widespread throughout the country. The disease devastated the country’s kiwifruit industry [38–40], and was projected to cost kiwifruit growers \$310 to \$410 million dollars for five years after the outbreak [41] due to a combination of fast spread and pathogen severity [42, 43]. Human-mediated transmission, caused by movement of infected materials between properties [19], contributes to this rapid spread since the bacteria can stay alive on machinery or tools [42]. Using this fact, our data-driven network-based spreading model is calibrated to this outbreak’s severity. We explore three different temporal aggregations of the network, similar to Bajardi *et al.* [33], to reflect horticulture industry seasonality. By using this calibrated model on seasonal networks, we illustrate that the month of pathogen importation strongly dictates epidemic size, peak, and onset time, demonstrating a direct link between movement seasonality and outbreak dynamics. This provides a practical guide to the development, calibration, and utilization of computational models that take advantage of human mobility data for predictive plant disease epidemiology, targeted surveillance, and biosecurity.

II. METHODS

A. Movement Data

We rely on data recorded by the Onside mobile app. The app is used by farmers and businesses servicing rural properties, such as contractors, processors, and other service providers. Data includes the information when users enter (“check-in”) one of the registered properties. Check-in events can either be recorded manually (i.e., a user checks in arriving at a property) or automatically (i.e., triggered by reaching the property boundaries based on digital geofence technology) and are associated with time stamps having a resolution of minutes.

Onside data contains information about individual properties, such as their area and geographical coordinates, and are classified based on their industry: horticulture, agriculture, and farming. Since we aim to model the Psa-V outbreak in New Zealand, we only focus on the $N = 2,281$ properties in the horticulture industry. A geographical map of the horticultural system in New Zealand reconstructed using Onside data is visualized in Figure 1.

From the Onside data at our disposal, we extract all $P = 86,624$ movements recorded between January 1, 2022, and December 31, 2022 (see Figure 2 for a schematic illustration). The data was pre-processed so time-stamps having a resolution of minutes are mapped to calendar months, since our epidemic model is calibrated on monthly timeseries data. As a consequence of such a rounding operation, the very same movement can appear multiple times in the data. Specifically, the p -th movement data is denoted by $z_p = (o_p, d_p, m_p)$, representing a person checking into property d_p in month

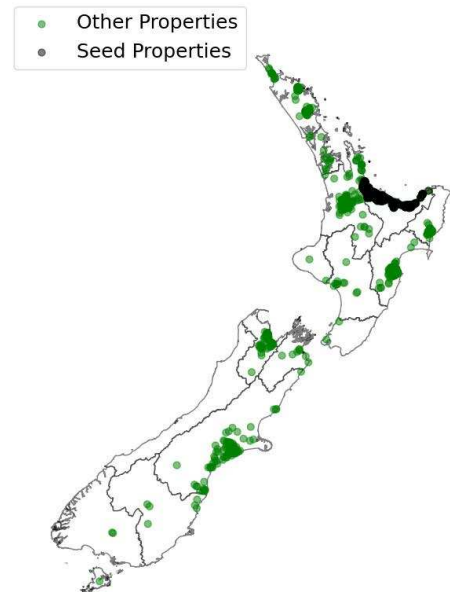


Figure 1. **Map of the horticulture industry in New Zealand.** Each point represents a property in the Onside dataset ($N = 2,281$ total properties). Black points denote the $S = 1,300$ properties located in the Bay of Plenty, which are used as seeds for the spreading dynamics simulated by our model.

m_p , with o_p representing the previous property where the very same person checked in. The indices o_p and d_p denote spatial units 1 through N ($N = 2,281$), while m_p corresponds to one of the twelve calendar months (January–December).

We construct directed and weighted networks of movements for each month, excluding all spurious movements having the same source and destination properties. The generic element of the weight matrix for month m is

$$\omega_{j \rightarrow i}^{(m)} = \frac{1}{30 \text{ days}} \sum_{p=1}^P \delta_{o_p, j} \delta_{d_p, i} \delta_{m_p, m} \quad (1)$$

where the Kronecker delta function is such that $\delta_{x, y} = 1$ if $x = y$ and $\delta_{x, y} = 0$ otherwise. $\omega_{j \rightarrow i}^{(m)}$ quantifies the average number of daily movements between properties j and i observed in month m .

In a similar way, we can generate directed and weighted networks of movements for 4 seasons: fall, winter, spring and summer. In such a case, the generic element of the weight matrix is

$$\omega_{j \rightarrow i}^{(s)} = \frac{1}{90 \text{ days}} \sum_{p=1}^P \delta_{o_p, j} \delta_{d_p, i} \delta_{f(m_p), s} \quad (2)$$

where $f(m)$ is the function that maps months to seasons, defined as follows: $f(m) = \text{fall}$ for $m = \text{March, April and May}$, $f(m) = \text{winter}$ for $m = \text{June, July and August}$, $f(m) = \text{spring}$ for $m = \text{September, October, November}$, and $f(m) = \text{summer}$ for $m = \text{December, January and February}$.

The yearly version of the network is instead given

$$\omega_{j \rightarrow i} = \frac{1}{365 \text{ days}} \sum_{p=1}^P \delta_{o_p, j} \delta_{d_p, i} \quad (3)$$

where all movements in the year are aggregated together.

A basic analysis of the constructed networks reveals that the volume of movements in the horticulture industry is highly seasonal; movements peak in the spring and summer seasons (highest in the months of February and November, shown in the inset of Figure 7 C), and reach the lowest numbers in winter (June and July). This aligns with horticulture industry labor trends, where employment peaks in the summer and is smallest in the winter months [44, 45].

In Table I, we show how the level of aggregation affects some basic network metrics. When calculating the metrics, we only consider the properties having at least one non-zero-weight incoming or outgoing edge. We then calculate the average values over the set of all graphs generated according to a specific level of temporal aggregation for the number of nodes $\langle N \rangle$, the number of edges $\langle E \rangle$, the first moment of the edges' weights $\langle \omega \rangle$, and the second moment of the edges' weights $\langle \omega^2 \rangle$.

By definition, the yearly network contains more nodes and edges than the monthly and seasonal networks. However, the weight of the connections is larger in the monthly and seasonal networks. This well aligns with an empirical understanding of how temporal networks exhibit ‘‘bursty’’ behavior with large amounts of activity occurring in a short period of time, followed by long periods of inactivity [46]. Estimates of the second moment highlight how, at all levels of aggregation, there is large heterogeneity in how the weights are distributed on the edges of the network.

Aggregation	$\langle N \rangle$	$\langle E \rangle$	$\langle \omega \rangle$	$\langle \omega^2 \rangle$
Yearly	2, 281	23, 418	0.01	0.84
Seasonal	1, 627	8, 124	0.03	0.80
Monthly	1, 153	3, 413	0.07	0.86

Table I. **Network statistics.** For each level of data aggregation, we report the corresponding average number of nodes $\langle N \rangle$, average number of edges $\langle E \rangle$, average value of the edges' weights $\langle \omega \rangle$ (measured in number of daily movements), and the second moment of the edge weight $\langle \omega^2 \rangle$.

B. Metapopulation Model

We are interested in developing a model for the spread of Psa-V that is calibrated on a timeseries quantifying the

monthly number of infected properties between February 2011 and March 2012, as collected by Greer and Saunders [41]. To this end, we make the strong assumption that the 2022 Onside data at our disposal can be used to generate networks of movements that are representative of both years 2011 and 2012. Specifically, we define the weight of the directed connection $j \rightarrow i$ at time t as

$$w_{j \rightarrow i}(t) = \begin{cases} \omega_{j \rightarrow i}^{(m=g(t))} & \text{monthly resolution} \\ \omega_{j \rightarrow i}^{(s=f(g(t)))} & \text{seasonal resolution} \\ \omega_{j \rightarrow i} & \text{yearly resolution} \end{cases} \quad (4)$$

In the above expression, $g(t)$ is the function that maps the model's time t to calendar months; $f(m)$ maps calendar months to seasons already used in Eq. (2).

The proposed metapopulation model combines two spreading mechanisms: within-property and between-property. Each property i , composed of H_i hectares of land, is represented as a population of susceptible and infected hectares. We denote the fraction of infected hectares on the property i at time t as $I_i(t)$ and the fraction of susceptible hectares for property i at time t as $S_i(t)$. By definition, we have that

$$S_i(t) + I_i(t) = 1, \forall i \in 1, \dots, N \text{ and } \forall t.$$

The level of transmission within a property is driven by the fraction of susceptible and infected hectares on that property (within-property transmission), and the importation of infection from other connected properties (between-property transmission). The equations describing the spread of the infection are:

$$\frac{dI_i(t)}{dt} = \beta_w I_i(t) S_i(t) \Theta [I_i(t) - I_i^{\min}] + \beta_b S_i(t) \sum_{j=1}^N w_{j \rightarrow i}(t) I_j(t) \Theta [I_j(t) - I_j^{\min}], \quad (5)$$

for $i = 1, \dots, N$. $\Theta(x)$ is the Heavyside function defined such that $\Theta(x) = 1$ if $x > 0$ and $\Theta(x) = 0$ otherwise. In Eq. (5), the force of infection within a property is denoted as β_w , and the force of infection between properties is denoted as β_b . To be considered infected and contribute to the spreading dynamics, property i must have a level of infection above the threshold I_i^{\min} where $I_i^{\min} = (H_i 625 \text{ plants hect}^{-1})^{-1}$; 625 is a realistic estimate of the average number of plants per hectare [47]. This threshold value is set to ensure that at least one plant in the property is infected before spreading occurs.

Eq. (5) is a mean-field approximation of the ground-truth spreading dynamics [48]. We assume that such an approximation well describes the average dynamical behavior of the system. We numerically integrate it using Newton's method (see Supplementary Materials for details). The initial condition at time $t = t_0$ is such that $I_i(t_0) = 0$ for all i except for a single seed property s_0 for which $I_{s_0}(t_0) = 0.1$. As shown in the Supplementary Materials, the results of our analysis are not much affected by the initial level of infection imposed for the seed property.

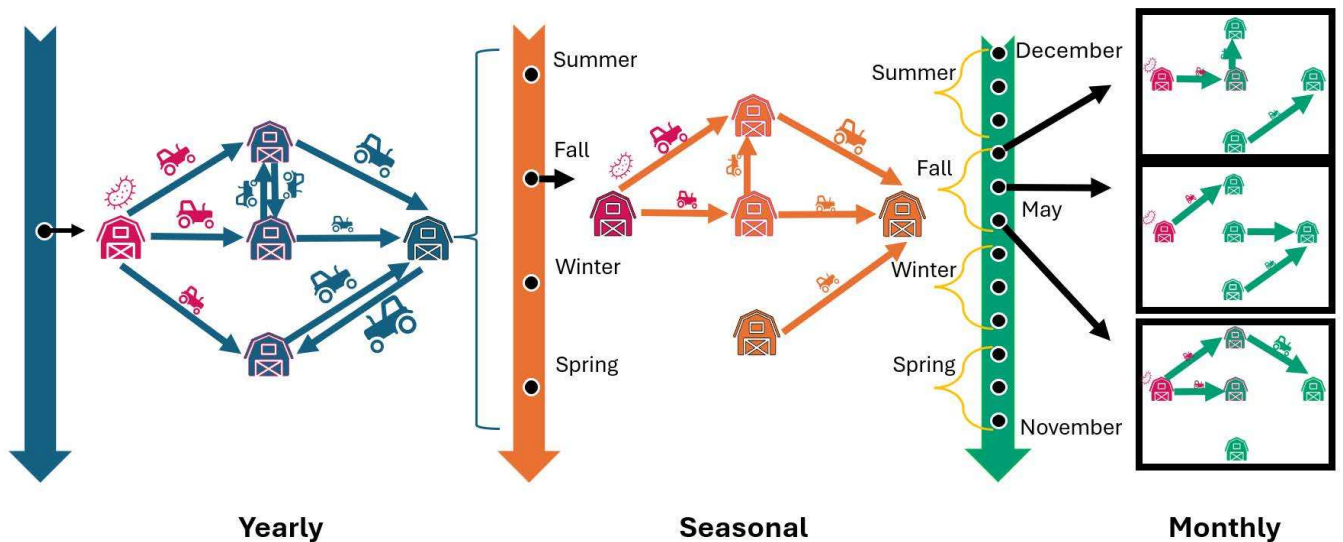


Figure 2. **Schematic representation of mobility networks.** Using the Onside movement dataset, we generate networks representing movements of workers between properties. In all networks, we measure the number of movements of people between properties, which vary based on the source and destination. A movement is directed in nature and is recorded when a person leaves a source property and checks into a destination property. In this figure, the size of the tractor corresponds to the number of movements: the larger the tractor, the more movements occur. Depending on the aggregation level of the data, we define either yearly, seasonal, or monthly networks. People moving between properties spread plant disease, and a higher frequency of movements between properties increases the probability of spreading. We note that starting the infection during different seasons or months can lead to different epidemic outcomes, since monthly movement networks differ. Infections are colored red showing how seeding infections during different seasons or months can lead to different epidemic pathways.

Unlike livestock disease, it can be difficult to detect early-stage symptoms of plant disease, in part, due to less routine monitoring. Thus, when monitoring the spread of the disease in our model, we require that $I_i(t) > D$ for the property i to be counted as infected at time t . We define the cumulative number of infections at time t measured in our model as:

$$O(t) = \sum_{i=1}^N \Theta [I_i(t) - D] . \quad (6)$$

We stress that the specific choice for the value of the detection threshold D does not affect how spreading unfolds, but only how spreading is monitored. D should be interpreted as an effective detection threshold, which combines the time it takes to detect and report symptoms as well as biological incubation.

C. Model Calibration

We use the data on the outbreak dynamics from a 2012 report by Greer and Saunders [41]. The report relies on infection records collected by Kiwifruit Vine Health (KVH), a biosecurity organization [38] responsible for protecting the kiwifruit industry from pests and disease. KVH was established in December 2010 to lead the response to the Psa-V incursion. As the KVH disaggregated data is not publicly available, we extract the

monthly values from the aggregated curve in the 2012 report using a plot digitizing tool [49]. The number of infected properties per growing season was detailed in Rosanowski *et al.* [50]; we use it to confirm the number of total infections in March 2012 in addition to the epidemic curve from Greer and Saunders [41].

The incidence curve shown in Fig. 3 details the observed total monthly infections from February 2011 to March 2012. Since infections had occurred before February 2011 [50], and the incidence in January 2011 and February 2011 was not available in the monthly dataset, the February data point is not included in our calibration procedure.

According to Rosanowski *et al.* [50], the largest spikes in infection occurred in the spring during 2011/2012 growing season and the spring of the 2012/2013 growing season, with the summer season having the second largest number of Psa-V infected properties. Symptom emergence is greatest in the spring for Psa-V due to the warm humid conditions and increased rainfall [42]. Although Psa-V symptoms are visually apparent once established, some orchards may have been infected earlier but only reported later due to biological latency, mild or ambiguous early symptoms, and limited awareness during the early outbreak phase. As an alternative reference curve for calibration, we also estimate a 2-month trailing moving average of the incidence curve. The moving average curve is calculated starting from February 2011 (see Supplementary Materials).

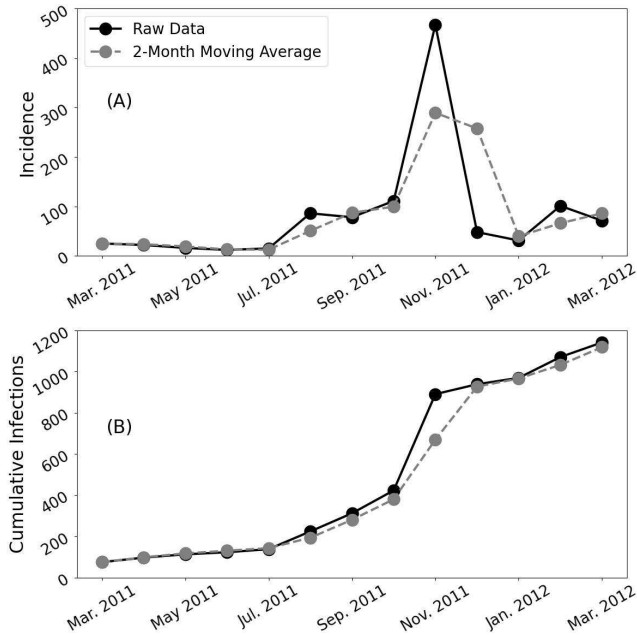


Figure 3. **Dynamics of the Psa-V epidemic in New Zealand.** (A) Number of new monthly infected properties and (B) cumulative number of monthly infected properties. The solid curve in both panels represents the raw data extracted from the report written by Greer and Saunders [41]. In this, the monthly infection data starts from February 2011 and ends in March 21st, 2012, but the actual outbreak started in November 2010 and has now become endemic in New Zealand. Thus, the leftmost point in the raw data corresponds to the number of properties that became infected between November 2010 and February 2011. The gray curve is a 2-month moving average of the raw timeseries. The moving average is calculated starting from March 2011.

The data used in our calibration procedure is given by 14 monthly counts of newly infected properties. We denote this timeseries as $\vec{x} = (x_1, x_2, \dots, x_{14})$, where we assume that data points are indexed in chronological order. This means that, for example, the index $c = 1$ refers to February 2011 and x_1 is the value of the incidence curve in February 2011, whereas the index value $c = 14$ refers to March 2012 and x_{14} is its corresponding value on the incidence curve. To compare the outcome of the metapopulation model with such real data, we discretize the timeseries of Eq. (6) by extracting a single value for each month from February 2011 to March 2012, i.e., $\vec{m} = (m_1, \dots, m_{14})$. Each of these values corresponds to the cumulative number of infections measured at the end of the corresponding month. For example, m_1 is the cumulative number of infections measured in the model at midnight of March 1st, 2011; m_{14} is instead the cumulative number of infections measured at midnight of April 1st, 2012. From the timeseries describing the cumulative number of infections, we immediately derive the incidence timeseries as $y_1 = m_1$ and $y_c = m_c - m_{c-1}$ for $c = 2, \dots, 14$.

Table II. **Model Parameters and their description.**

Parameter	Description
R	Temporal resolution for the movement network
β_w	Within-property transmission rate
β_b	Between-property transmission rate
s_0	Initial seed property
t_0	Initial time of the spreading process
D	Detection threshold

The outcome of the metapopulation model depends on six tunable parameters, see Table II. In our calibration procedure, we assume that the dynamics starts on November 1st, 2010, thus effectively bringing down the number of free parameters to five [41, 50]. More simply, our model runs for four months before we compare incidence to the real data.

For each level of temporal aggregation, we perform a grid search to find the best-fitting values for the other model parameters (β_w, β_b, D, s_0), which we detail in more depth in the Supplementary Materials. Potential configurations are filtered using the heuristic criterion detailed below in Equation 7. Note that we run separate calibrations for the different levels of temporal aggregation of the movement data. Also, note that, still relying on evidence from prior literature [41, 50], we allow seed nodes to be taken only from the set of properties in the Bay of Plenty, see Figure 1, as the outbreak originated from that region. The goal of the calibration is to ensure that the resulting dynamics fits available incidence data with an acceptable level of uncertainty, a common goal of other disease models [51].

Given a configuration θ of the free model parameters and an aggregation R , we numerically integrate the Eqs. (5) of the metapopulation model to generate the incidence curve $\vec{y}(\theta) = (y_1(\theta), \dots, y_{14}(\theta))$. Such a configuration is considered viable, i.e., $\theta \in V$, if

$$|x_c - y_c(\theta)| < \max\{30, 0.8x_c\} \quad (7)$$

for all $c = 2, \dots, 14$. The above is a heuristic criterion that allows us to select only configurations of the model's parameters whose outcome is compatible with the ground truth in the entire observation window for the data at our disposal. In the Supplementary Materials, we plot the percentage of viable configurations while varying these two heuristic values in a heatmap. From that, we chose 30 and 0.8 in the criterion above as they were the first two values with more than 0 viable configurations for all aggregations, when using the raw data. We use this criterion to prevent overfitting to any one specific month and filter any configurations that do not exhibit similar growth trends to the incidence data. Among all viable configurations, we identify the best configuration $\hat{\theta}$ as the one minimizing the root mean squared error (RMSE), i.e.,

$$\hat{\theta} = \arg \min_{\theta \in V} \sqrt{\frac{\sum_{c=2}^{14} (x_c - y_c(\theta))^2}{13}} \quad (8)$$

Note that in both Eqs. (7) and (8), we start from the index $c = 2$ thus excluding the first data point in the timeseries. This same procedure is also used to determine the values of the model parameters that best fit the 2-month moving average of the incidence curve, Table III.

D. Spatiotemporal characterization of the spreading dynamics

Our metapopulation model of Eq. (5) allows us to keep track of the level of infection $I_i(t)$ of each property i at time t . Similarly to what was described in the previous section, we discretize such a continuous timeseries into 14 values $\vec{m} = (m_1^{(i)}, \dots, m_{14}^{(i)})$ each value corresponding to the months between February 2011 and March 2012. We define the time to detect infection for property i , namely c_i^* , as the minimum value of the index c for which $m_c^{(i)} > D$. We finally measure the monthly detection distance d_i^* between i and the closest property j such that $c_j^* = c_i^* - 1$. Since multiple properties can be detected at the same time c^* , we compute the minimum, mean, and maximum of the quantity d^* for all properties that are first detected as infected at time c^* .

Similarly, we estimate the distance between property i , first infected at time c_i^* , and each of the connected properties j that are first infected at time $c_j^* = c_i^* - 1$. We refer to this quantity as the contact distance $d_{i,j}$. For each value c^* , multiple values of the contact distance may be observed; thus, we compute the minimum, mean, and maximum of the contact distance for all properties that are first detected as infected as functions of c^* .

These distance metrics allow us to track whether the outbreak distance radically changes over time. The contact distance metric tells us the distance that newly infected properties have from their infectors, while the outbreak distance metric sheds light on the distance that newly infected properties have from one another. The latter metric gives information on how the front of the epidemic expands, month by month.

III. RESULTS

A. Replicating observed spreading dynamics

In Table III, we report the values of the best estimates of our model. They are grouped based on the level of data aggregation; also, we display separate results depending on whether the reference timeseries is based on the raw incidence data or their moving average. Two nice aspects are apparent from our estimates. First, their values are very robust across the various levels of aggregation, with the within-property contribution being about three times larger than its between-property counterpart. Second, as show in the Supplementary Materials, their posterior distributions are well peaked around their mode.

Data	Aggregation	β_b	β_w	D
Raw	Monthly	0.03	0.09	0.4
	Seasonal	0.03	0.08	0.8
	Yearly	0.04	0.07	0.8
Moving Average	Monthly	0.02	0.10	0.4
	Seasonal	0.03	0.07	0.8
	Yearly	0.02	0.10	0.4

Table III. **Best-fitting parameter values.** Best-fitting parameter values for each temporal aggregation using the raw and moving average incidence data. We use bold-face fonts to highlight the best-fitting aggregation level for each type of reference curve.

We visually compare the incidence curves from the raw data and the model estimates corresponding to the best fit for the three different levels of temporal aggregation in Figure 4A. The bands for each of the model's curves represent the uncertainty of the incidence estimates due to the choice of the seed s_0 when using the best-fitting parameter values for β_w, β_b, D given the temporal aggregation and incidence curve. Within the insets of Figure 4, we compute the total percentage of viable configurations in V and the percentage of unique seeds observed given the best-fitting values for β_b, β_w and D for all levels of temporal aggregation. A similar analysis is considered in Figure 4B, the model is fit against the 2-month moving average of the incidence curve.

The results shown in Figure 4 illustrate that the model is able to capture epidemic dynamics well for all levels of temporal aggregation. The model seems to better fit the 2-month moving average of the incidence curve rather than its raw version. The difficulty of fitting well the raw incidence timeseries arises from the extreme steepness of the outbreak peak, with doubling time being less than the available data time step (1 month). This highlights the need for higher temporal disaggregation of infection data for the calibration of the proposed model when highly transmissible pathogens are analyzed.

Of all levels of temporal aggregations, the seasonal configuration provides the best fit, i.e., smallest RMSE [Eq. (8)], for the dynamics of the observed incidence (Fig. 4A). It also has the largest percentage of seeds for its best-fitting configuration, but the smallest percentage of viable configurations. For the 2-month moving average epidemic curve (Fig. 4B), the monthly network provides the best fit. Compared to the observed incidence, the percentage of viable configurations and best-fitting seeds is greater than for the 2-month moving average across temporal aggregations. The root mean-squared error values are smaller for the best-fitting configurations for the moving average compared to the raw data. This indicates that the model struggles less with smoother dynamics when doubling time is comparable (or preferably) shorter than the temporal observational scale.

The model is well calibrated in terms of outbreak timing, with the correct peak month being captured per-

fectly by all levels of temporal aggregations, both for the raw incidence curve and its moving average. Additionally, the best-fitting seasonal model calibrated for raw incidence captures not only the peak that occurs in November 2011 but also the second incidence increase that occurs in February 2012.

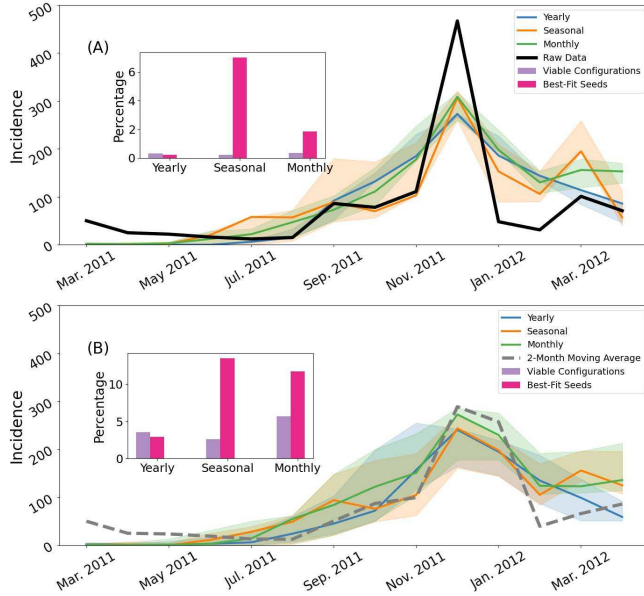


Figure 4. **Best-fitting epidemic models.** (A) We plot the incidence timeseries obtained from the epidemic model when setting its parameter values to their corresponding best estimates. Different colors refer to different levels of temporal aggregation of the movements between properties: yearly (blue), seasonal (orange), and monthly (green). The shaded areas define the uncertainty associated with each of these curves, computed by taking the minimum and maximum values of the incidence measured over the viable seeds for the best-fitting values for β_b, β_w, D . Model’s curves are compared against raw data (black). The inset displays the percentage of viable configurations for the parameters in violet, as well as the percentage of unique seeds appearing in the best-fitting configuration when holding β_b, β_w, D to their best fitting value. This analysis was conducted for the various levels of temporal aggregation that can be in the model. (B) Same as in (A), but obtained when fitting the model against the 2-month moving average incidence curve (gray dashed).

B. Spatial Spread

As seen in Figure 5, most spreading events are initially local. Over 90% of all newly infected properties are less than 10 km from their closest infectors (see SM), illustrating the dominance of local spread. However, rare long-distance events pull the average distance between newly infected properties and another closest infected property into the range of 10–100 km (Fig. 5). This feature is a direct result of the movement network’s spatial structure, with most movements between properties

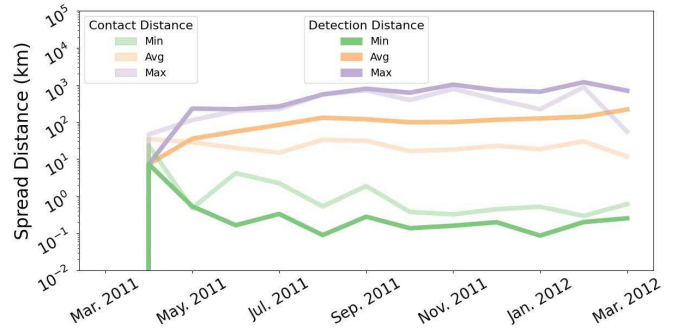


Figure 5. **Spatio-temporal characterization of the spreading.** Two distance metrics are compared using three different statistics: the mean, minimum, and maximum. The detection-distance metric is calculated by comparing the distances of all properties that are infected within the same month. The contact distance is calculated by finding the average distance of a newly infected property’s contacts. A contact is defined as a previously infected property that has an outgoing link to the newly infected property. We define a newly infected property as one that is detected as infected, not simply if it can transmit infection.

(71.3%) being short-range ($< 10\text{km}$), 12.2% of movements being $> 20\text{km}$ and rare cases reaching 1,000 km (the CCDF of the movement distribution is shown in the SM). Moreover, the importance of such movements for transmission increases as the outbreak continues. This is illustrated by the average distance from the closest infected property consistently increasing each month. The heterogeneity of the distance between infected contacts and newly infected nodes also increases with time due to two factors: (i) the number of close susceptible nodes decreases, and (ii) the pathogen reaches close but less connected properties (a smaller number of movements). This leads to initially small and local outbreak spreading far beyond its origin. In the SM, we plot how the cumulative infection distance from the initial seed grows over time. Tracking the outbreak from the source of infection, the infection spreads more than 1,000 km from where it is seeded. We observe that growth from the seed occurs in a staggered manner, where every 2 – 3 months there is an increase in distance from the seed property.

C. Experimental Analysis

1. Detection threshold

The detection threshold D is the minimum fraction of infected hectares that must be present on a property for it to be considered infected. The larger D is, the more hectares must become infected for a property to be observed as infected, see Eq. (6). Figure 6 shows the temporal dynamics of the outbreak for different D values; we use the network constructed using seasonal aggregation of movement data, and set all the model’s parameters

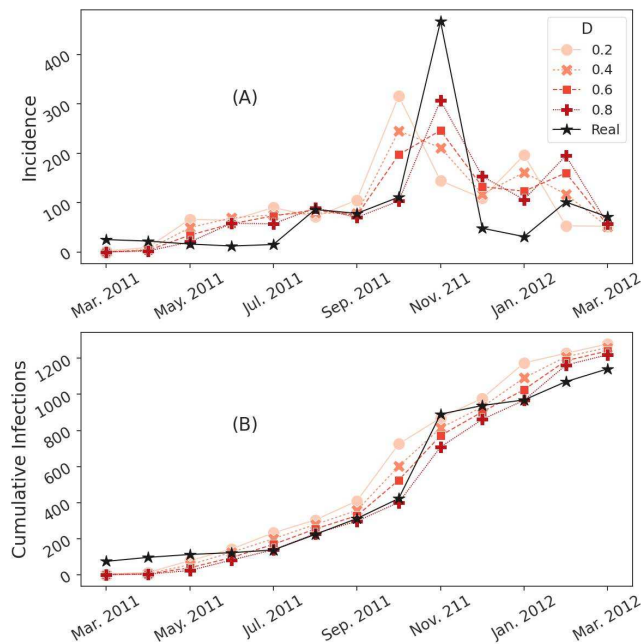


Figure 6. **Dependence of the model's outcome on the detection threshold.** We vary the detection threshold D and plot the effect this has on the incidence curve in panel (A) and on the cumulative total infections shown in panel (B). The best fitting parameter configuration is $D = 0.8$ for the seasonal network. In panel (A), we plot the raw incidence curve as a reference, and in panel (B), the raw cumulative infection data are plotted. For all graphs, the seasonal network is used as well as the corresponding parameters of the best fit, Table III.

to their best-fitting values (Table III, and Figure 4A). Decreasing D effectively allows us to observe outbreak occurrence earlier.

Despite the peak incidence shifting by one month, the model illustrates similar temporal dynamics for different detection thresholds. The magnitude of incidence is similar when comparing the smallest and largest values, and the final outbreak size only differs by 2.7%, decreasing from 56.1% of properties for $D = 0.2$ to 53.4% for $D = 0.8$. This illustrates that, without implemented interventions, early detection does not substantially affect the observed final size of the outbreak or the height of the peak incidence.

2. Importation month

All the above analysis was conducted using the realistic assumption that the importation month was November 2010. Now, we consider hypothetical scenarios where the time of pathogen importation may occur at the beginning of each calendar month during the year. For each month, we integrate the equations of the metapopulation model using the best estimates of the model's parameters for the monthly aggregation, see Table III. To make the various

scenarios comparable, the equations are integrated for the same total amount of time of 14 months. When the hypothetical importation month is set to November, we obtain very similar initial conditions to those used in all previous results, though we only run this experiment for 365 days compared to the calibrated model.

To evaluate the impact of the timing of pathogen importation, we consider four different metrics characterizing the spread of the epidemic: (i) the overall number of infections (Fig. 7A), (ii) the peak incidence value (Fig. 7B) as well as (iii) the time when such a peak is reached (Fig. 7D), (iv) the effective start of the epidemic which we define as the first instant of time when at least two properties are detected as infected (Fig. 7C). The number of total movements per month is shown as well (inset of Fig. 7C), and we compare the cumulative infections/incidence trends against the number of movements per month. All metrics were calculated by seeding infection from properties within the Bay of Plenty. The variation in distributions occurs due to the differences in the first movement network associated with the different importation months.

Every month, there is a fraction of seeds where the final outbreak size is smaller than 250 infections. In May-July, this fraction increases together with an overall decrease in outbreak size heterogeneity, resulting in a smaller median final outbreak size. Our results show that the biggest outbreak sizes are observed when importation occurs in March and April, i.e., the months with the maximum number of movements.

We observe that importations in the fall and winter months lead to a higher incidence at the peak of the outbreak, with the highest variability in May through August - similar to the cumulative infections distributions. There exists a consistently higher probability of the outbreak either not taking off or remaining very small in winter, reflected in similar trends for the final outbreak size and peak incidence. However, for the combination of epidemiologic parameters and importation seeds resulting in bigger outbreaks, peak incidence tends to be highest for winter importations and lowest for summer importations. With the median final outbreak size being the highest for fall importations and lowest for winter importations, this suggests different spatiotemporal dynamics for the importations in different seasons.

Finally, we see that the onset (2 – 4 months) and peak (7 – 8 months) times are almost constant irrespective of the value of the importation month. We also find that it takes longer for outbreaks to peak (Fig. 7B) and start (Fig. 7C) if they begin in the fall or winter seasons.

IV. DISCUSSION

We use a metapopulation model that incorporates human movements to simulate plant disease spread. Our model reproduces the dynamics of the Psa-V outbreak that occurred starting from 2010 in New Zealand, demon-

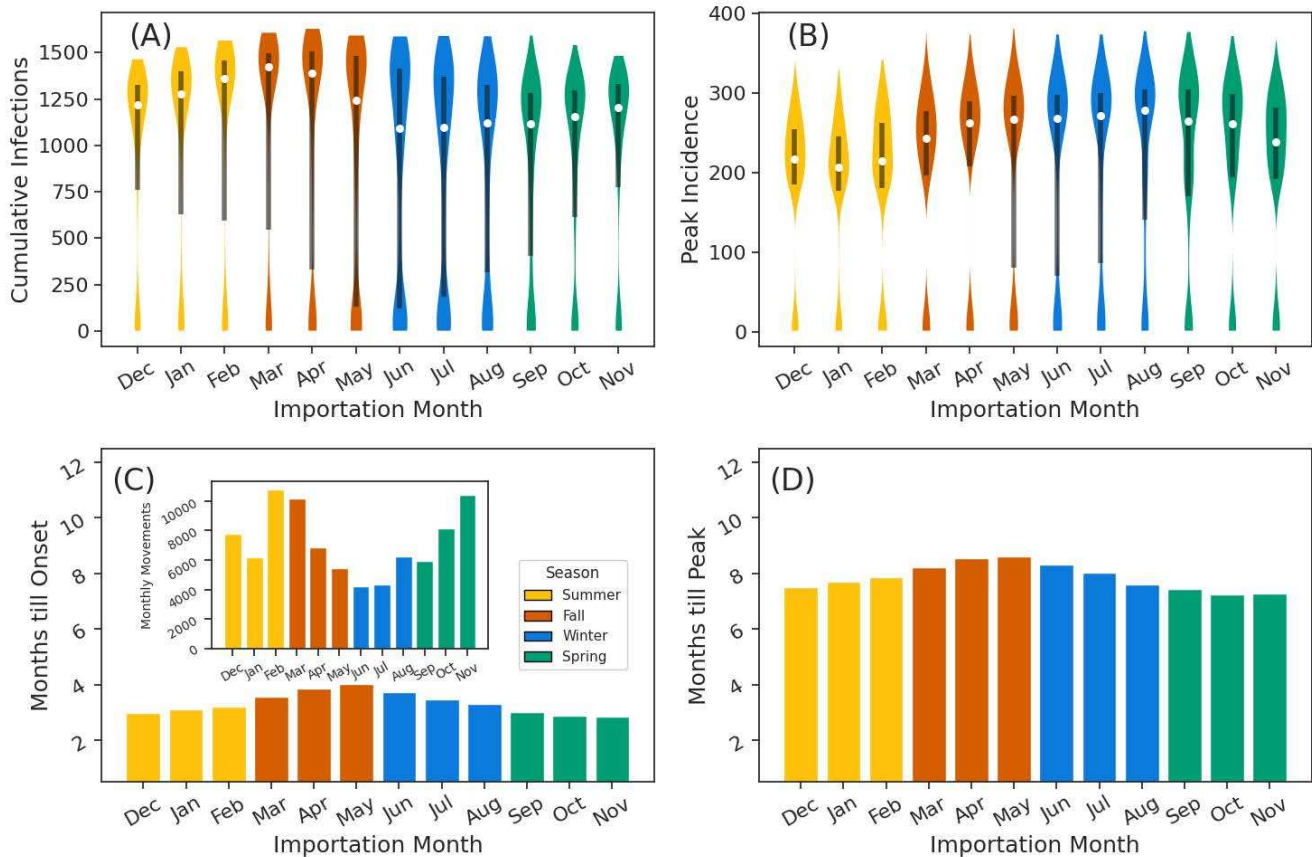


Figure 7. **Dependence of the model's outcome on importation month.** (A) The distribution of the final outbreak size (violin plots) for each importation month. Black boxes show the 50% inter-quartile range. White circles show the median value. (B) As in (A), but for the distribution of peak incidence. (C) The mean number of months from importation until the month of peak incidence. In the inset, the total number of movements per month is plotted. (D) The mean number of months from importation until the onset (time when 2 infected farms are detected). Colors of bars and violins denote seasons.

strating that the movements of people can be effectively utilized to model the spread of plant disease. The metapopulation model relies on underlying mobility networks generated by aggregating movement data over time windows of variable length, i.e., monthly, seasonal, and yearly time windows. While all of them approximate the infection dynamics well, the seasonal network fits the infection dynamics from the raw data best. This occurs since farm work is seasonal, so a seasonal resolution is sufficient to capture most movement complexity.

Results from our model provide critical quantitative insights for biosecurity. We show that disease mostly spreads locally between properties, within a radius of about 10 km, a finding supported by the literature [50]. However, nationwide outbreaks can quickly occur due to rare long-distance movements leading to sudden jumps in spread distance. Due to this combination of short-range spreading events and rare long-distance jumps, plant disease outbreaks always have the potential to spread over large distances if the disease is not detected quickly enough.

Our model also allows us to test the sensitivity of disease spreading to initial conditions. Detecting infection on a property depends on the intensity of monitoring efforts, and we find that increasing sensitivity to detecting infection could represent an effective surveillance strategy. Also, we find that the median size of the outbreak increases if disease is imported during months with many movements. At parity of importation time, the specific location where the disease is imported contributes to the large variability in epidemic severity. Some seed properties generate only small and local outbreaks, and some others cause system-wide epidemic events.

This work is one of the first to use the movements of people to simulate the spatio-temporal spread of plant diseases. Other works have focused on how environmental factors [4, 30] or farm proximity [32] affect plant disease spread. By contrast, we show that the movement network of people strongly affects the size and speed of an outbreak, with epidemic dynamics changing depending on the initial seed location. Here, we directly harness the movement of people to model disease spread, allowing

surveillance strategies to be directly related to real movement patterns. If a novel plant disease begins to spread in New Zealand, the calibrated model could be used as a helpful tool to test different potential scenarios.

Worker movements are tied to the growing season, so the density of movements per property changes based on how busy properties are by season. This highlights the importance of modeling how the movement network changes in time, since the temporality strongly affects the distribution of movements. The horticulture industry could leverage this knowledge to use different outbreak management strategies for different seasons. More generally, this model could help forecast a plant disease outbreak in the short-term, since the calibration grounds the estimates in a past real-world outbreak, help decision makers plan for new outbreaks, or assess options during an ongoing one.

While our model can provide insights into the impact of human movements on the spread of plant disease, our work has several limitations. Our model has not been extended to account for the impact of specific climatic variables such as humidity, rainfall, and wind. For parameter identifiability purposes, we focus our work on human mobility networks; however the model is flexible enough to adapt a more complex mechanism for within and between property spread.

Additionally, the monthly observed infection data that we used to calibrate the model were affected by active interventions that were occurring at the time to prevent Psa-V spread [38, 41]. The infection data was collected based on symptom emergence, rather than the identification of infection. Further access to the individual property level data was limited, therefore model validation was based on aggregated monthly infection data.

In a similar fashion, access to daily or weekly incidence data was limited. Such access would allow for aggregation of the movement data at finer temporal resolution.

When calibrating the model, we utilized the full New Zealand horticulture movement network to simulate the spread of Psa-V, a kiwifruit disease. The 2010 outbreak was larger than the number of kiwifruit growing properties in the horticulture movement network. Utilizing only present day kiwifruit properties would result in underestimation of the historical outbreak data. The full horticulture movement network was used to give a fuller representation of the mobility network compared to only

using the kiwifruit network.

When evaluating the calibrated model, we observe that our model underestimates the full magnitude of the peak incidence for the raw data across all aggregations. In contrast, our model well captures the peak incidence for the moving average data across all aggregations. This suggests that model performance is more sensitive to data type than aggregation choice.

While this study effectively illustrates the calibration pipeline using a straightforward filtering and RMSE approach, the framework is designed to be adaptable, allowing future research to incorporate traditional inference methods like Markov-chain Monte-Carlo methods [52] or particle filtering[53].

This model offers several promising avenues for future research. A primary focus is identifying which properties function most effectively as sentinel nodes [34, 54] to ensure the timely detection of outbreaks. Beyond surveillance, this modeling framework can also be used to evaluate various containment strategies to mitigate disease spread once an outbreak is identified.

V. DATA AVAILABILITY

All the code and data needed to reproduce the results of the study are available on Github here: https://github.com/vakrao/net_plant_spread. Due to the potential identifiability of individual properties, the latitude and longitude coordinates associated with each property will not be released publicly. Access to the location data should be requested from Onside.

VI. ACKNOWLEDGMENTS

This project was supported by the Onside company via a collaborative grant. We would like to thank Reza Shoorangiz and Zach Hitchcock from Onside for their help. The company had no role in study design, data analysis, the decision to publish, or any opinions, findings, and conclusions or recommendations expressed in the manuscript. F.R. acknowledges partial support by the Air Force Office of Scientific Research under award number FA9550-24-1-0039.

-
- [1] H. Fielder, T. Beale, M. J. Jeger, G. Oliver, S. Parnell, A. M. Szyniszewska, P. Taylor, and N. J. Cunliffe, *Phytopathology* **114**, 1717 (2024).
 - [2] A.-L. Laine, *Current Biology* **33**, R574 (2023).
 - [3] J. Yuen and A. Mila, *Annual Review of Phytopathology* **53**, 471 (2015).
 - [4] M. Cendoya, A. Navarro-Quiles, A. López-Quílez, A. Vicent, and D. Conesa, *Journal of Agricultural, Biological and Environmental Statistics* (2024), 10.1007/s13253-024-00604-2.
 - [5] S. Orozco-Fuentes, G. Griffiths, M. Holmes, R. Ettelaie, J. Smith, A. Baggaley, and N. Parker, *Ecological Modelling* **393**, 12 (2019).
 - [6] C. Landry, C. Abadie, F. Bonnot, and J. Vaillant, *International Journal of Computer Applications* **174**, 1 (2021).
 - [7] M. T. Signes-Pont, J. J. Cortés-Plana, H. Mora, and R. Mollá-Sirvent, *Kybernetes* **50**, 2943 (2020), publisher:

Emerald Publishing Limited.

- [8] S. M. White, J. M. Bullock, D. A. Hooftman, and D. S. Chapman, *Biological Invasions* **19**, 1825 (2017).
- [9] P. M. Severns, *Life* **12**, 1727 (2022).
- [10] D. Chapman, F. Occhibove, J. M. Bullock, P. S. Beck, J. A. Navas-Cortes, and S. M. White, *PLOS Computational Biology* **21**, e1013539 (2025).
- [11] Y. F. Suprunenko, S. J. Cornell, and C. A. Gilligan, *Royal Society open science* **12**, 240763 (2025).
- [12] D. Shah, P. Paul, E. De Wolf, and L. Madden, *Philosophical Transactions of the Royal Society B* **374**, 20180273 (2019).
- [13] D. H. Gent, S. Bhattacharyya, and T. Ruiz, *Phytopathology* **109**, 1392 (2019).
- [14] H. K. Adrakey, G. J. Gibson, S. Eveillard, S. Malembic-Maher, and F. Fabre, *PLoS Computational Biology* **19**, e1011399 (2023).
- [15] A. Varghese, C. Drovandi, A. Mira, and K. Mengersen, *PLoS Computational Biology* **16**, e1007878 (2020).
- [16] L. Rimbaud, C. Bruchou, S. Dallot, D. R. Pleydell, E. Jacquot, S. Soubeyrand, and G. Thébaud, *Royal Society Open Science* **5**, 171435 (2018).
- [17] G. A. Forster and C. A. Gilligan, *Proceedings of the National Academy of Sciences* **104**, 4984 (2007).
- [18] W. Ocimati, A. F. Tazuba, and G. Blomme, *Frontiers in Agronomy* **3**, 655824 (2021).
- [19] C. Hardy and C. Kvh, (2013).
- [20] D. J. Hodkinson and K. Thompson, *Journal of Applied Ecology* , 1484 (1997).
- [21] J. B. Ristaino and M. L. Gumpertz, *Annual Review of Phytopathology* **38**, 541 (2000).
- [22] M. Pautasso and M. J. Jeger, *AoB Plants* **6**, plu007 (2014).
- [23] M. Marshall, R. Sutherland, and P. E. Hulme, *Australasian Plant Pathology* **50**, 671 (2021).
- [24] K. Andersen, C. E. Buddenhagen, P. Rachkara, R. Gibson, S. Kalule, D. Phillips, and K. Garrett, *Phytopathology* **109**, 1519 (2019).
- [25] M. Moslonka-Lefebvre, A. Finley, I. Dorigatti, K. Dehnen-Schmutz, T. Harwood, M. J. Jeger, X. Xu, O. Holdenrieder, and M. Pautasso, *Phytopathology* **101**, 392 (2011).
- [26] Y. Benedetti and F. Morelli, *PLOS ONE* **12**, e0183691 (2017), publisher: Public Library of Science.
- [27] E. Numminen and A.-L. Laine, *PLOS Computational Biology* **16**, e1007703 (2020).
- [28] M. J. Jeger, M. Pautasso, O. Holdenrieder, and M. W. Shaw, *New Phytologist* **174**, 279 (2007).
- [29] D. E. Aylor, *Ecology* **84**, 1989 (2003).
- [30] J. K. Brown and M. S. Hovmöller, *Science* **297**, 537 (2002).
- [31] S. Suttrave, C. Scoglio, S. A. Isard, J. S. Hutchinson, and K. A. Garrett, *PLoS One* **7**, e37793 (2012).
- [32] G. Strona, C. J. Carstens, and P. S. Beck, *Scientific Reports* **7**, 71 (2017).
- [33] P. Bajardi, A. Barrat, F. Natale, L. Savini, and V. Colizza, *PloS one* **6**, e19869 (2011).
- [34] P. Bajardi, A. Barrat, L. Savini, and V. Colizza, *Journal of the Royal Society Interface* **9**, 2814 (2012).
- [35] E. Valdano, C. Poletto, A. Giovannini, D. Palma, L. Savini, and V. Colizza, *PLoS computational biology* **11**, e1004152 (2015).
- [36] F. Schirdewahn, H. H. Lentz, V. Colizza, A. Koher, P. Hövel, and B. Vidondo, *Plos one* **16**, e0244999 (2021).
- [37] V. Colizza and A. Vespignani, *Journal of theoretical biology* **251**, 450 (2008).
- [38] D. Birnie and A. Livesey, Sapere Research Group Limited, Wellington, New Zealand (2014).
- [39] J. L. Vanneste, *Annual Review of Phytopathology* **55**, 377 (2017).
- [40] K. Froud, N. Cogger, and R. Beresford, *New Zealand Plant Protection* **67**, 34 (2014).
- [41] G. Greer and C. M. Saunders, (2012).
- [42] K. Froud, K. Everett, J. Tyson, R. Beresford, and N. Cogger, *New Zealand Plant Protection* **68**, 313 (2015).
- [43] A. Cameron and V. Sarojini, *Plant pathology* **63**, 1 (2014).
- [44] Food and Fibre Centre of Vocational Excellence, *Seasonal Workforce Analysis: Report Outline (Final)*, Technical Report (Food and Fibre Centre of Vocational Excellence, 2025).
- [45] J. Timmins and S. N. Zealand, *Seasonal employment patterns in the horticultural industry* (Statistics New Zealand Wellington, 2009).
- [46] A. Sheng, Q. Su, A. Li, L. Wang, and J. B. Plotkin, *Nature Communications* **14**, 7311 (2023).
- [47] New Zealand Kiwifruit Growers Inc., *New Zealand Kiwifruit Book 2024* (New Zealand Kiwifruit Growers Inc., 2024) accessed: 2025-04-08.
- [48] R. Pastor-Satorras, C. Castellano, P. Van Mieghem, and A. Vespignani, *Rev. Mod. Phys.* **87**, 925 (2015).
- [49] “Plotdigitizer: Version 3.1.6,” (2025).
- [50] S. Rosanowski, T. Carpenter, M. Stevenson, and K. Froud, Report prepared for Zespri International Ltd and Kiwifruit Vine Health, Massey University, Palmerston North, New Zealand , 34 (2013).
- [51] S. Merler, M. Ajelli, L. Fumanelli, M. F. Gomes, A. P. y Piontti, L. Rossi, D. L. Chao, I. M. Longini, M. E. Halloran, and A. Vespignani, *The Lancet Infectious Diseases* **15**, 204 (2015).
- [52] G. Chowell, *Infectious Disease Modelling* **2**, 379 (2017).
- [53] W. Yang, A. Karspeck, and J. Shaman, *PLoS computational biology* **10**, e1003583 (2014).
- [54] E. Colman, P. Holme, H. Sayama, and C. Gershenson, *PLoS computational biology* **15**, e1007517 (2019).

Modeling plant disease spread via high-resolution human mobility networks

Supplementary Materials

Varun K. Rao,^{1,2} Ryan Higgs,³ Hautahi Kingi,³ Filippo Radicchi,¹ Santo Fortunato,¹ and Maria Litvinova^{2,*}

¹*Center for Complex Networks and Systems Research,
Luddy School of Informatics, Computing, and Engineering,
Indiana University, Bloomington, Indiana 47408, USA*

²*School of Public Health, Indiana University, Bloomington, Indiana 47408, USA*

³*Onside, Christchurch, New Zealand.*

* malitv@iu.edu

I. NUMERICAL INTEGRATION OF THE MEAN-FIELD APPROXIMATION

Denote with $I_i(t)$ the fraction of hectares that are infected in farm i at time t , and with $S_i(t)$ the fraction of hectares that are not infected in farm i at time t . We clearly have $I_i(t) + S_i(t) = 1$ for all $i = 1, \dots, N$ and all $t \geq 0$.

The farm-based mean-field equations for the SI dynamics are

$$\frac{dI_i(t)}{dt} = \beta_w I_i(t) S_i(t) \Theta [I_i(t) - I_i^{\min}] + \beta_b S_i(t) \sum_{j=1}^N w_{j \rightarrow i}(t) I_j(t) \Theta [I_j(t) - I_j^{\min}] , \quad (\text{S1})$$

where β_w and β_b are the transmission rates within and between farms, respectively. $\Theta(x)$ is the Heavyside function defined such that $\Theta(x) = 1$ if $x > 0$ and $\Theta(x) = 0$ otherwise. To be considered infected and contribute to the spreading dynamics, property i should have a level of infection that is above the threshold $I_i^{\min} = (H_i 625 \text{ plants hect}^{-1})^{-1}$, where 625 is a realistic estimate of the average number of plants per hectare [1]. $\omega_{j \rightarrow i}^{(m)}$ quantifies the average number of daily movements between properties j and i observed in month m .

We can also write the above as a finite-difference equation

$$I_i(t + dt) = I_i(t) + \beta_w dt I_i(t) S_i(t) \Theta [I_i(t) - I_i^{\min}] + \beta_b dt S_i(t) \sum_{j=1}^N w_{j \rightarrow i}(t) I_j(t) \Theta [I_j(t) - I_j^{\min}] \quad (\text{S2})$$

To perform the numerical integration, we require that

$$\beta_w dt I_i(t) S_i(t) \Theta [I_i(t) - I_i^{\min}] + \beta_b dt S_i(t) \sum_{j=1}^N w_{j \rightarrow i}(t) I_j(t) \Theta [I_j(t) - I_j^{\min}] \leq 1 - I_i(t) . \quad (\text{S3})$$

leading to the constraint for the time increment:

$$dt \leq \frac{1 - I_i(t)}{\beta_w I_i(t) S_i(t) \Theta [I_i(t) - I_i^{\min}] + \beta_b S_i(t) \sum_{j=1}^N w_{j \rightarrow i}(t) I_j(t) \Theta [I_j(t) - I_j^{\min}]} . \quad (\text{S4})$$

Such a condition means that Eq. (S2) can effectively be used to numerically integrate Eq. (S1). Since the above must be true for all farms, we need to impose

$$dt \leq \min \left(T_{\text{inc}}, \min_{i=1, \dots, N} \frac{1 - I_i(t)}{\beta_w I_i(t) S_i(t) + \beta_b S_i(t) \sum_{k=1}^N \frac{w_{k \rightarrow i}}{\tau} I_k(t)} \right) . \quad (\text{S5})$$

where $T_{\text{inc}} = 1$ to generate at least one data point per day.

II. INFECTION DATA

The number of monthly cumulative infections and incidence from the 2010 Psa-V outbreak in New Zealand was digitized from Greer and Saunders [2] and is listed in Table S1. Raw data values are shown as well as the values for the trailing 2-month moving average. Using this incidence data we calibrated our model.

TABLE S1. Monthly raw counts and two-month moving average (MA(2)) incidence and cumulative infections.

Month	Raw Counts		2 Month Moving Average	
	Incidence	Cumulative	Incidence	Cumulative
Feb. 2011	50	50	50	50
Mar. 2011	25	75	25	75
Apr. 2011	22	97	23.5	98.5
May. 2011	16	113	19	117.5
Jun. 2011	10	123	13	130.5
Jul. 2011	15	138	12.5	143
Aug. 2011	86	224	50.5	193.5
Sep. 2011	88	312	87	280.5
Oct. 2011	111	423	99.5	380
Nov. 2011	467	890	289	669
Dec. 2011	48	938	257.5	926.5
Jan. 2012	31	969	39.5	966
Feb. 2012	101	1070	66	1032
Mar. 2012	71	1141	86	1118

III. GRIDSEARCH CALIBRATION

The model contains four free parameters which require calibration: the within-property spreading rate β_w , the between-property spreading rate β_b , the detection threshold D , and the initial seed property s_0 . We test 1,300 different seed properties located in the Bay of Plenty region and test several different values of the detection threshold D , where set $D = \{0.2, 0.4, 0.6, 0.8\}$.

To find an appropriate range of values for β_w and β_b , we first conducted a coarse exploratory gridsearch using logarithmic increments and searched over $[10^{-3}, 10^0]$. For each pair of dynamical parameters, (β_w, β_b) , the average RMSE was calculated using all values of D and s_0 . The RMSE landscape shown in Figure S1 indicates that the best parameter configurations are between $[10^{-2}, 10^{-1}]$ for all combinations of β_w, β_b , taking into account different data types and temporal aggregations. Informed by this finding, we performed a finer-grained gridsearch varying β_w, β_b (Figure S2 over the range $[10^{-2}, 10^{-1}]$ using increments of 0.01 across the set values of D and s_0 .

$$|x_c - y_c(\theta)| < \max\{\epsilon, z * x_c\} \quad (\text{S6})$$

The average RMSE values shown in both gridsearches (Fig S1 and Fig S2) were calculated across the set of configurations G , consisting of all possible combinations of β_b, β_w, D, s_0 that were discussed for each gridsearch. Given G , and each configuration entry θ for all free parameters, we filtered configurations using the heuristic defined in the main text to prevent overfitting to the incidence curves.

We slightly redefine the filtering heuristic in Equation S6, using ϵ and z as the two main variables that need to be set when performing the filtering. ϵ is utilized as a tolerance value while z is the size of our uncertainty band. In the main text, $\epsilon = 30$ and $z = 0.8$. A gridsearch was conducted to find the best values for ϵ and z using the raw data in Figure S3. ϵ was varied from $10^1 - 10^2$ in increments of 10^1 while z was varied from $10^{-1} - 1$ in increments of 10^{-1} . The percentage of viable configurations that existed by fulfilling the conditions in Equation S6 was recorded for each combination. From that gridsearch, $\epsilon = 30$ and $z = 0.8$ are the first two values that produce the smallest percentage of viable configuration among all aggregations. See the main text for details on how we selected the best configuration for each aggregation type.

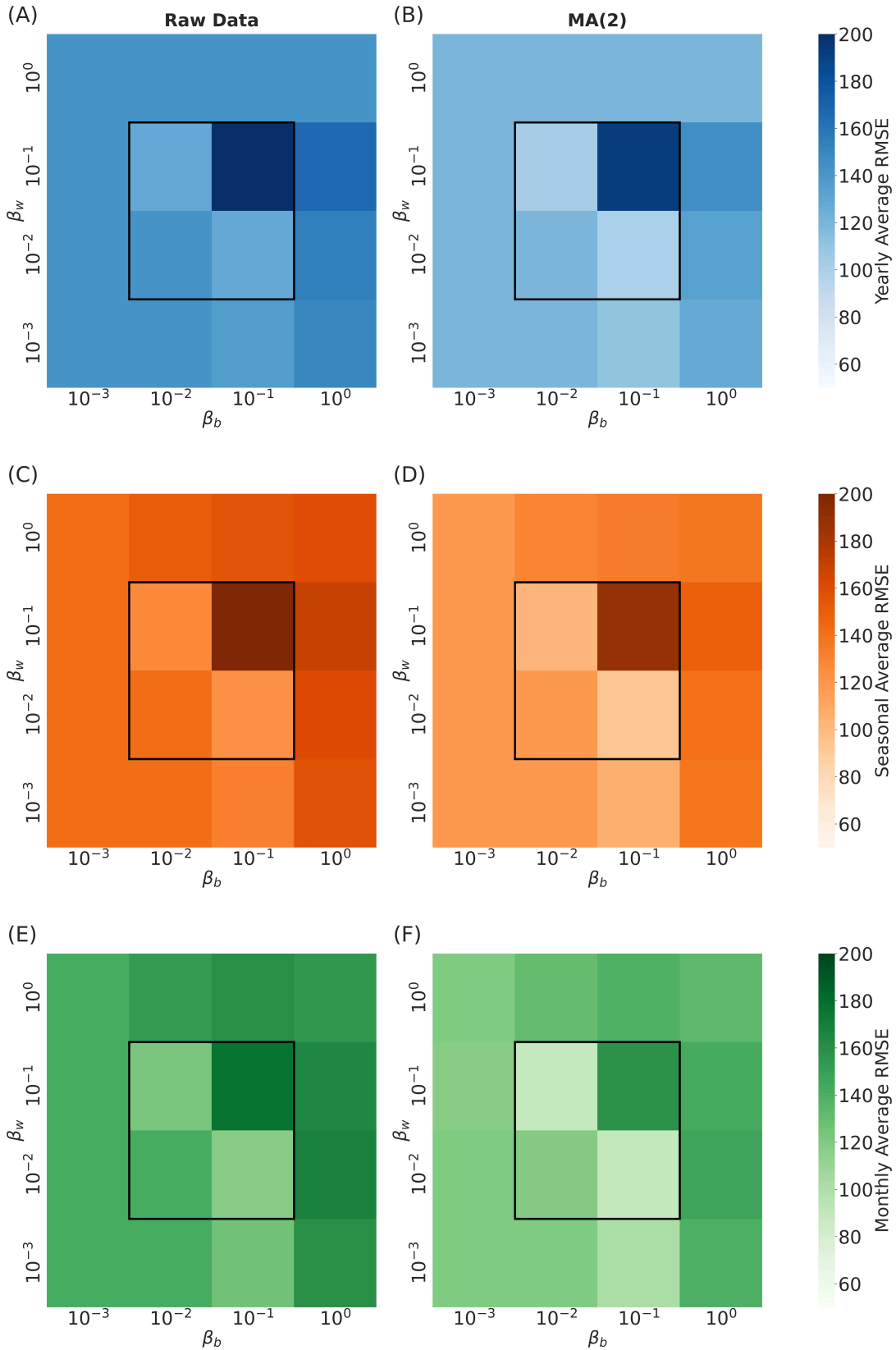


FIG. S1. **Logarithmic gridsearch calibration of β_b, β_w** We present the average RMSE for the various combinations of (β_w, β_b) where we vary the values for these dynamical parameters from 10^{-3} to 10^0 in logarithmic increments. Each square in the heatmap is the expected RMSE value for the joint distribution of β_w and β_b over all the possible s_0 and D combinations. The black square within each heatmap represent the values for β_b, β_w that were searched for in more depth in the linear gridsearch used in the main text. The RMSE values in the first column of heatmaps is calculated with reference to the raw data, while the values in the second column are calculated with respect to the two month moving average (MA(2)) data. In panel (A) we plot the RMSE for the yearly aggregation using the real data, in panel (B) we plot the average RMSE for the yearly network aggregation using the MA(2) data, in panel (C) we plot the average RMSE for the seasonal network aggregation using the raw data. while in panel (D) we plot the average RMSE for the seasonal aggregation using the MA(2) data. In panel(D) and (F) we plot the average RMSE for the monthly aggregation using the raw incidence data and MA(2) incidence data respectively.

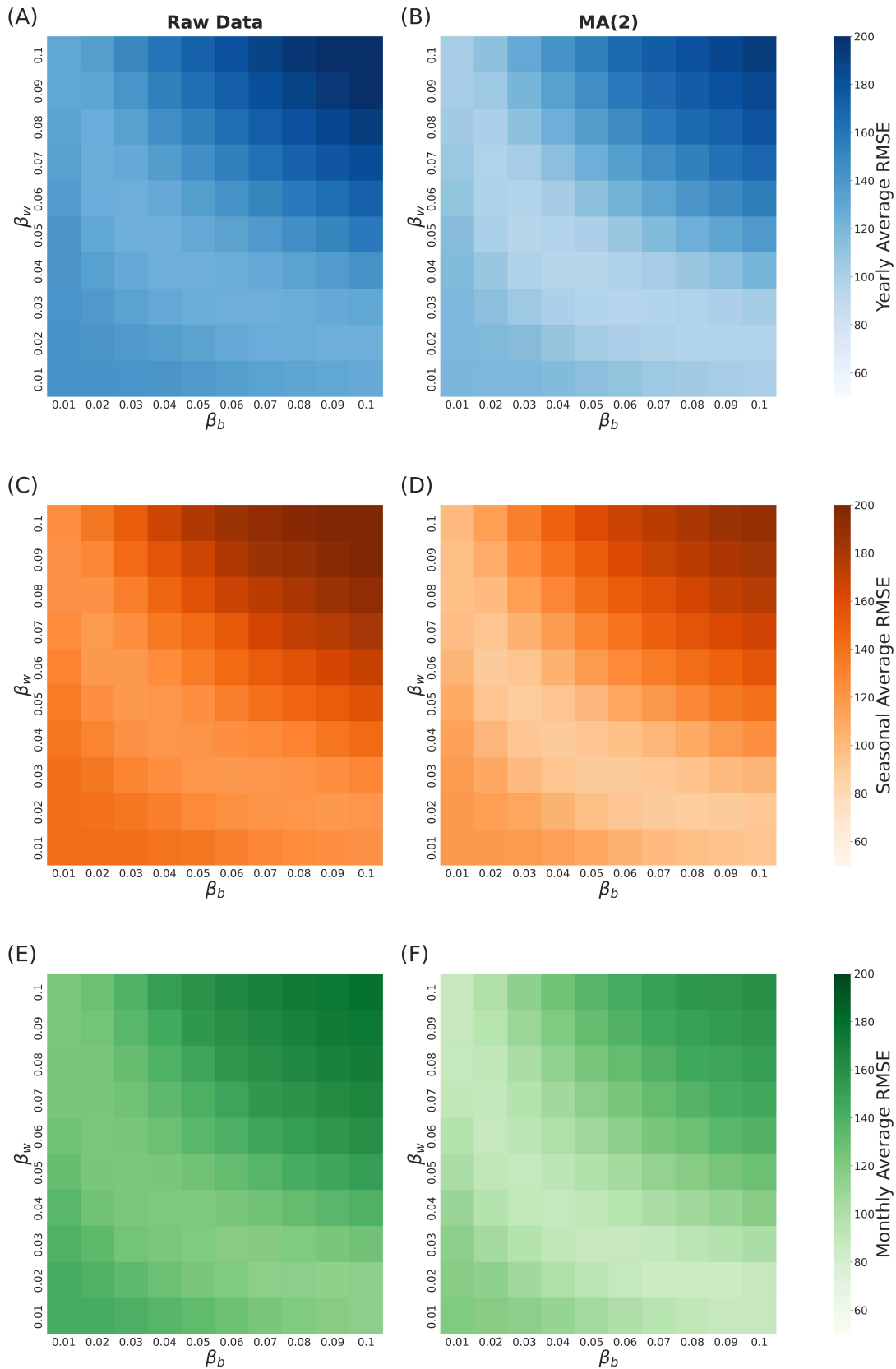


FIG. S2. **Linear gridsearch calibration of β_b, β_w** Similar to Figure S1 we plot the average RMSE for combinations of (β_w, β_b) , where RMSE values in the first column of the heatmaps are calculated with reference to the raw data, while the values in the second column are calculated with reference to the MA(2) data. We vary the values for these dynamical parameters from 10^{-2} to 10^{-1} respectively, in increments of 10^{-1} .

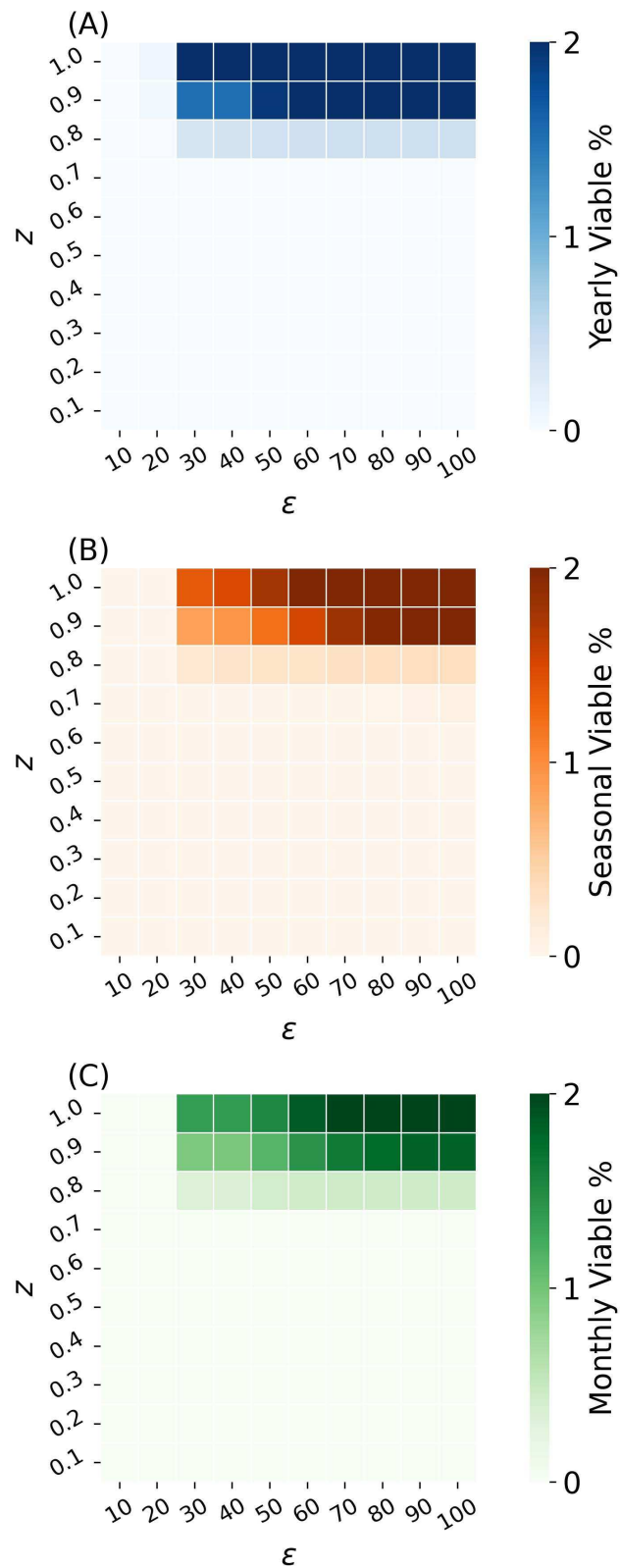


FIG. S3. **Parameter gridsearch for ϵ and z .** The parameter values for ϵ and z are varied here. We show the results of three different gridsearches, for all aggregations, using the raw data for the incidence curve to determine the . The darker the square in the heatmap, the higher percentage of viable configurations exist for that specified combination of ϵ and z . Panel (A) reports the percentage of viable configurations for the yearly aggregation, (B) and (C) are the same as (A) except for the seasonal and monthly aggregations respectively.

Using the viable configurations for each aggregation and data type, we plot the posterior distribution of the parameters in Figure S4. We observe that there are strongly preferred values for all parameters and aggregations, barring the monthly aggregation for the raw data. For β_w and β_b , specific values are clearly preferred. For the monthly raw aggregation, there is a bimodal distribution.

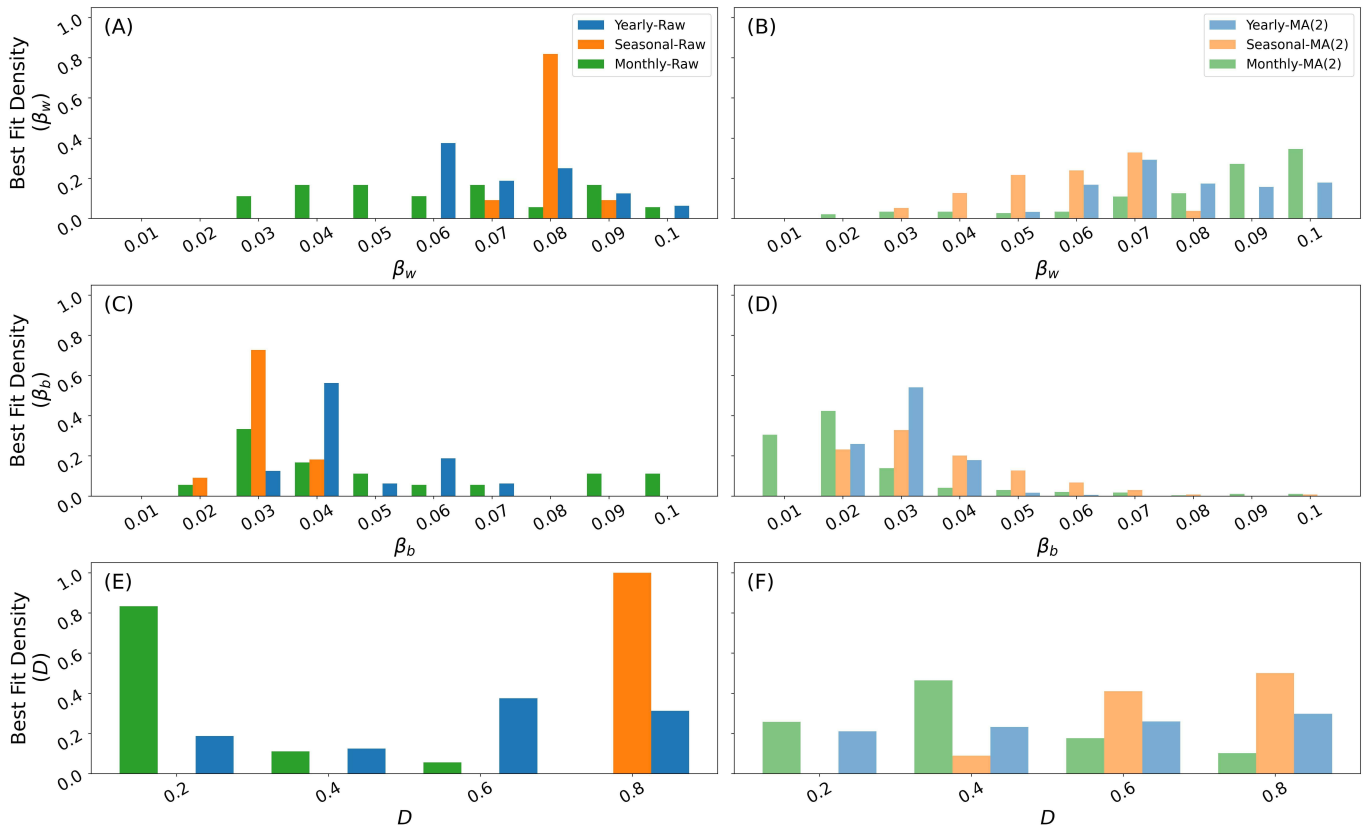


FIG. S4. **Posterior Distribution of Linear Gridsearch** Using the RMSE values generated from the linear gridsearch, seen in Fig. S2, we plot the posterior distribution for each parameter (except the seed, due to the number of seeds). These distributions are generated after creating the viable configuration set V for each aggregation and data type (Raw and MA(2) incidence data) and limiting the viable configurations to the configurations that have the smallest 1% of RMSE values among all configurations V . The best-fitting configurations are found from the configurations in V that minimize the RMSE best for each configuration and data type. The first column RMSE values are calculated with reference to the raw data, while the second column RMSE values are calculated with reference to the MA(2) data. Three different colors are used in each panel to reference different network aggregations. Blue represents the yearly aggregation, orange represents the seasonal aggregation, and green represents the monthly aggregation. Each row contains the posterior distribution for a different parameter. Panels (A) and (B) plot the distribution for β_w , panels (C) and (D) plot the distribution for β_b , and panels (E) and (F) plot the distribution for D . The RMSE values in panels (A), (C) and (E) are computed with respect to the raw data while in panels (B), (D), and (F) they are calculated using the MA(2) data.

IV. SPATIAL SPREAD

The complementary cumulative distribution function (CCDF) of movement length (i.e., distance between origin and destination property) is calculated and shown in Fig. S5. 99.1% of movements occur between properties that are between 0 – 100 km from each other, with 71.2 % of movements occurring having a distance of 10 km. From such a movement distribution, we can conclude that most movements in horticulture movement network occur between properties that are relatively close to one another. This movement structure leads to the results in Figure S6 where newly infected properties are infected within 10 km of another previously infected property. While most movements are short-distance, long distance spread from the seed still occurs, as we find in Figure S7, where by the end of the outbreak the epidemic has spread more than 1,000 km from where it started.

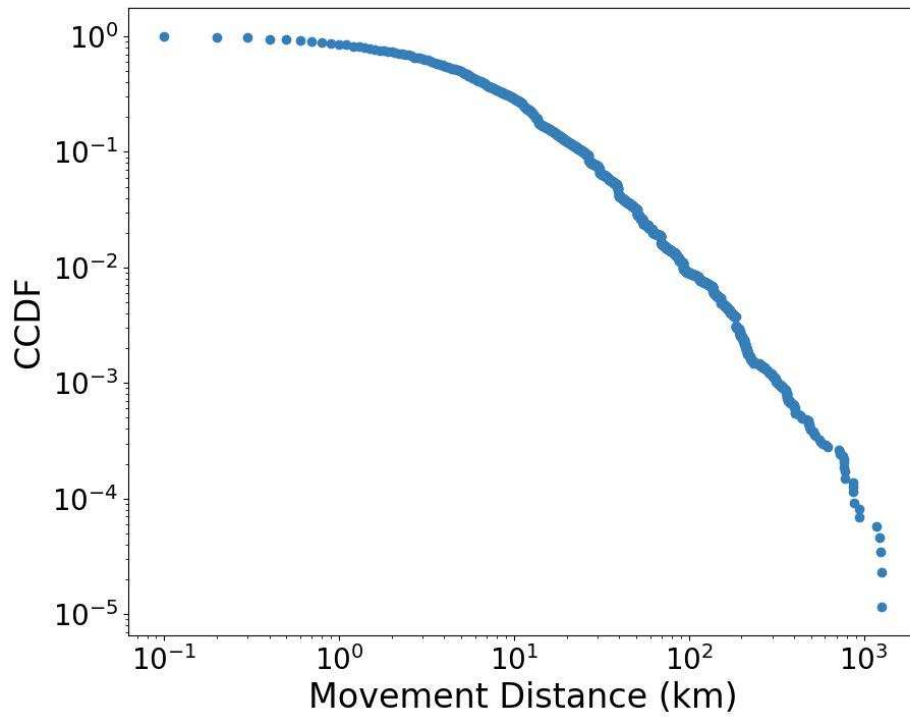


FIG. S5. CCDF of Movement Length.

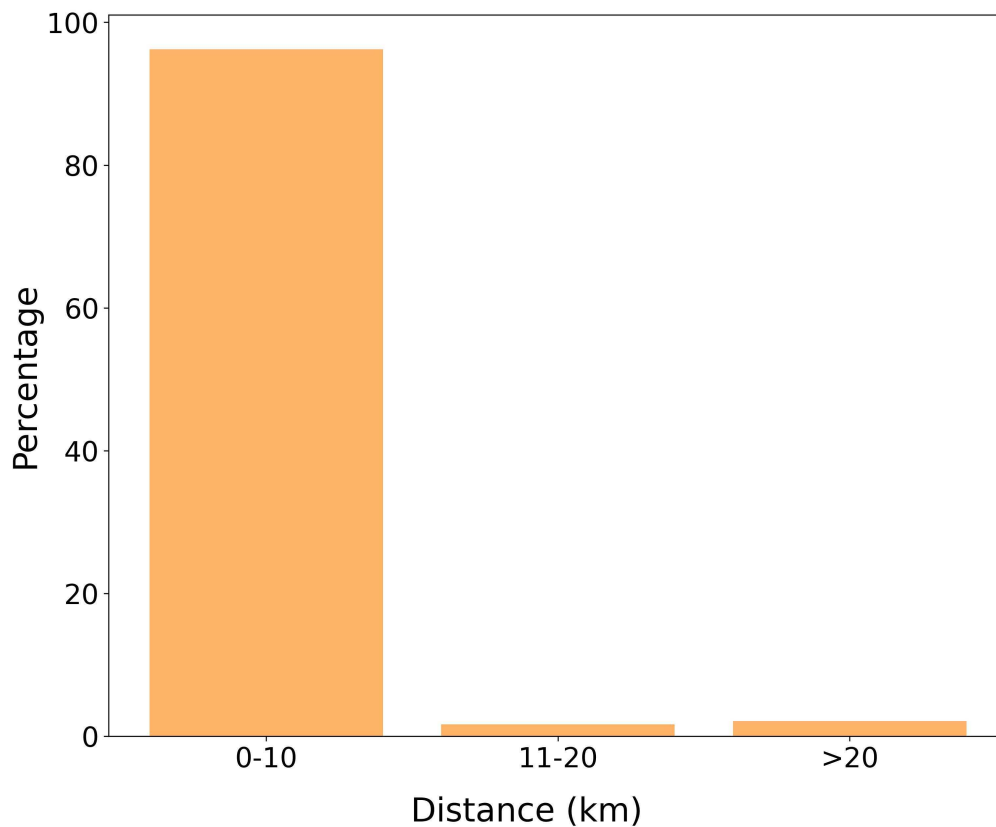


FIG. S6. **Distance of Newly Infected Property to the Closest Infected Property** Once a property becomes infected we measure the distance in kilometers from that property to the closest infected property. An infected property i is defined as one where the level of infection on it exceeds D where $I_i > D$. We classify this distance using three categories: 0 – 10 km, 11 – 20 km, and > 20 km. Most newly infected properties are within 0 – 10 km of a previously infected property, and only 2.7% of properties are > 20 km away from an infected property.

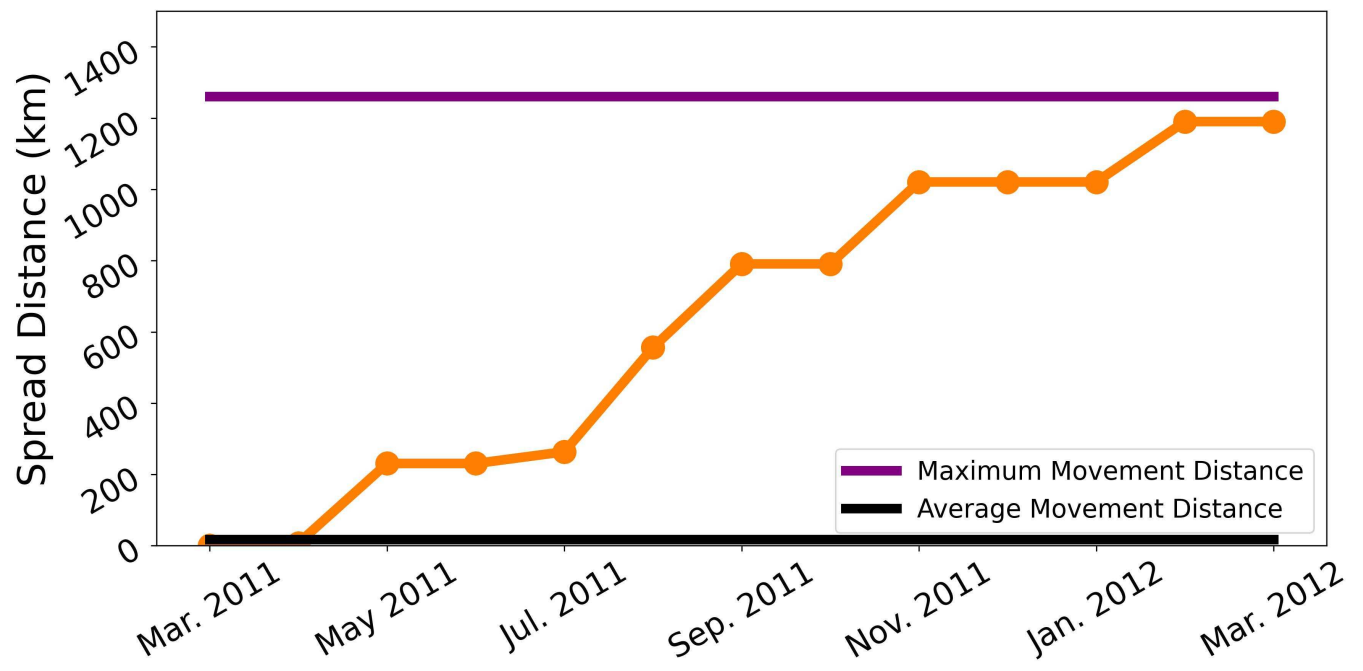


FIG. S7. **Maximum Spread Distance from Seed** Using the calibrated seasonal model, we plot the largest geodesic distance an infected property has from the initially infected seed property s_0 . We define this distance as the spread distance. The node with the largest distance away from the seed could persist for months, as we observe that for consecutive months at a time the spread distance does not change in value. As reference, we plot the maximum and average movement distance between any two properties as well. By the end of the outbreak, the distance from the seed is very close to the maximum existing movement distance.

V. VARYING INITIAL SEED VALUE

We calibrate the model assuming that the seed property's (s_0) infection level (I_{s_0}) is set to 0.1. Figure S8 shows the temporal dynamics of the outbreak when the initial amount we infect the seed with, I_{s_0} , is varied. We denote I_{s_0} as α for this experiment. We vary α using the calibrated model based on the seasonal network. When calibrating the model $\alpha = 0.1$, and find that increasing α increases the size of the outbreak while not having a large effect on the incidence dynamics. This result highlights the small effect that α has on outbreak size, and how it does not have a large effect on outbreak dynamics.

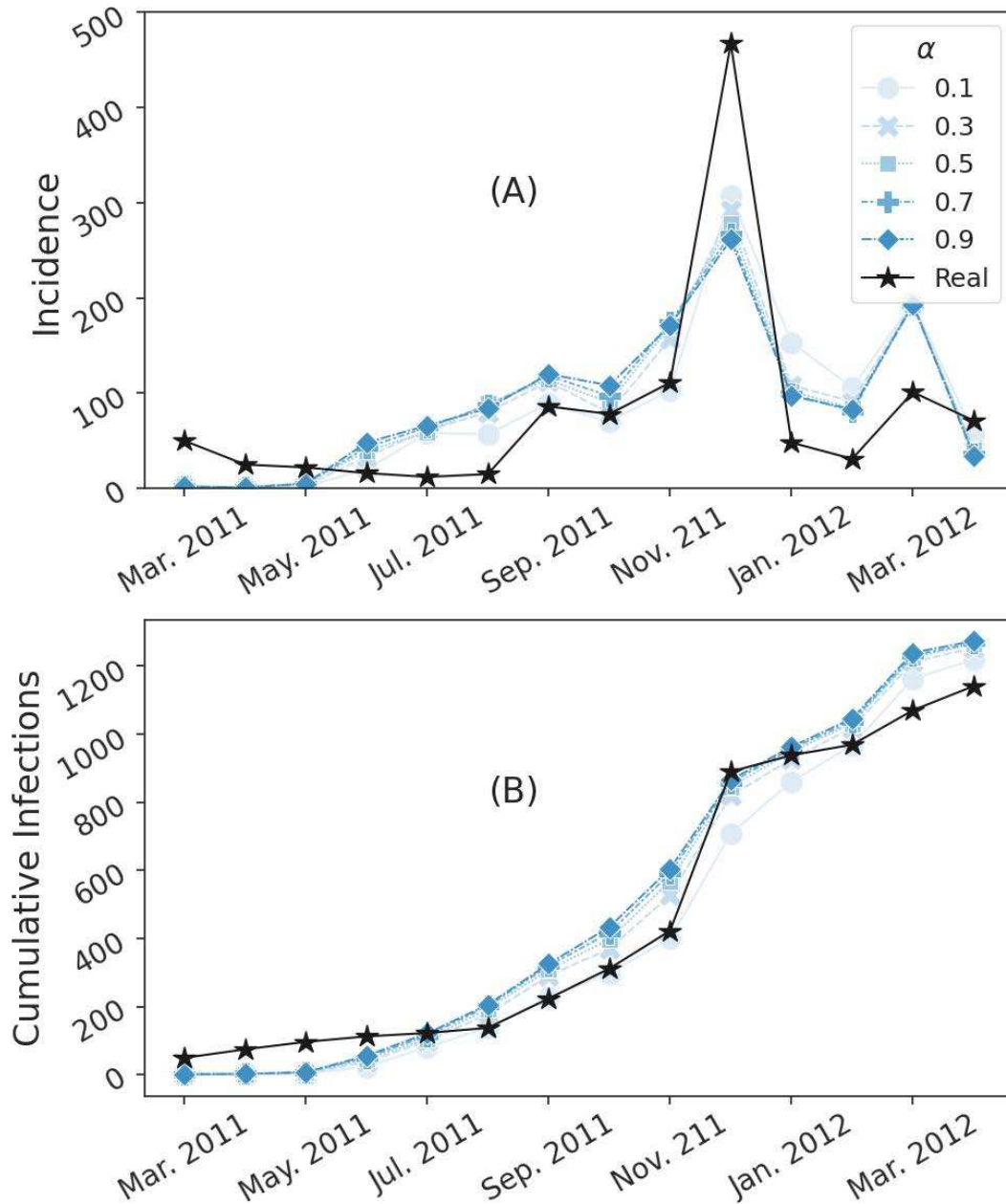


FIG. S8. **Dependence of Model's Outcome on Initial Seed Value** We vary the initial seed value α and plot the effect this has on the incidence curve in panel (A) and on the cumulative total infections shown in panel (B). We set $\alpha = 0.1$ when calibrating the model. Here we vary α from 0.1 to 0.9 in increments of 0.2 in both panels. In panel (A) we plot the real incidence curve as a reference, and in panel (B) the real cumulative infection data is plotted. For all graphs, the seasonal network is used as well as the corresponding parameters of best fit

-
- [1] New Zealand Kiwifruit Growers Inc., *New Zealand Kiwifruit Book 2024* (New Zealand Kiwifruit Growers Inc., 2024) accessed: 2025-04-08.
- [2] Glen Greer and Caroline M Saunders, "The costs of psa-v to the new zealand kiwifruit industry and the wider community," (2012).